



**HAL**  
open science

## Polymorphism of benzylthiouracil, an active pharmaceutical ingredient against hyperthyroidism

Ivo B. Rietveld, Hassan Allouchi, Maria Barrio, René Ceolin, Josep-Lluis Tamarit

### ► To cite this version:

Ivo B. Rietveld, Hassan Allouchi, Maria Barrio, René Ceolin, Josep-Lluis Tamarit. Polymorphism of benzylthiouracil, an active pharmaceutical ingredient against hyperthyroidism. *International Journal of Pharmaceutics*, 2021, 598, pp.120378. 10.1016/j.ijpharm.2021.120378 . hal-03166420

**HAL Id: hal-03166420**

**<https://normandie-univ.hal.science/hal-03166420>**

Submitted on 10 Mar 2023

**HAL** is a multi-disciplinary open access archive for the deposit and dissemination of scientific research documents, whether they are published or not. The documents may come from teaching and research institutions in France or abroad, or from public or private research centers.

L'archive ouverte pluridisciplinaire **HAL**, est destinée au dépôt et à la diffusion de documents scientifiques de niveau recherche, publiés ou non, émanant des établissements d'enseignement et de recherche français ou étrangers, des laboratoires publics ou privés.



Distributed under a Creative Commons Attribution - NonCommercial 4.0 International License

---

# POLYMORPHISM OF BENZYLTHIOURACIL, AN ACTIVE PHARMACEUTICAL INGREDIENT AGAINST HYPERTHYROIDISM

Ivo B. Rietveld<sup>1,2\*</sup>, Hassan Allouchi<sup>3</sup>, Maria Barrio<sup>4</sup>, René Ceolin<sup>4</sup>, Josep-Lluis Tamarit<sup>4</sup>

<sup>1</sup> Normandie Université, Laboratoire SMS - EA 3233, Université de Rouen, F 76821 Mont Saint Aignan, France

<sup>2</sup> Faculté de Pharmacie, Université de Paris, 4 avenue de l'observatoire, 75006, Paris, France

<sup>3</sup> EA SIMBA: Synthèse et Isolement de Molécules BioActives, Laboratoire de Chimie Physique, Faculté de Pharmacie, 31, avenue Monge - 37200 Tours, France

<sup>4</sup> Grup de Caracterització de Materials, Departament de Física and Barcelona Research Center in Multiscale Science and Engineering, Universitat Politècnica de Catalunya, EEBE, Campus Diagonal-Besòs, Av. Eduard Maristany 10-14, 08019 Barcelona, Catalunya, Spain

\* Corresponding author: [ivo.rietveld@univ-rouen.fr](mailto:ivo.rietveld@univ-rouen.fr). Current address: Neutron Science Laboratory, Institute for Solid State Physics, University of Tokyo, 5-1-5 Kashiwanoha, Kashiwa, Chiba 277-8581, JAPAN

## 20 ABSTRACT

21 The crystal structures of dimorphic benzylthiouracil, a drug against hyperthyroidism, have been redetermined  
22 and the atom coordinates of the two independent molecules of form I have been obtained for the first time.  
23 The dimorphism convincingly demonstrates the conformational versatility of the benzylthiouracil molecule. It  
24 has been established through calorimetric studies that the low-temperature form II transforms  
25 endothermically ( $\Delta_{II \rightarrow I}H = 5.6(1.5) \text{ J g}^{-1}$ ) into form I at 405.4(1.0) K. The high-temperature form I melts at  
26 496.8(1.0) K ( $\Delta_{I \rightarrow L}H = 152.6(4.0) \text{ J g}^{-1}$ ). Crystallographic and thermal expansion studies show that form I is  
27 denser than form II, leading to the conclusion that the slope of the II-I equilibrium curve in the pressure-  
28 temperature phase diagram is negative. It follows that this dimorphism corresponds to a case of overall  
29 enantiotropic behaviour, which implies that both solid phases possess their own stable phase region  
30 irrespective of the pressure. Moreover, form II is clearly the stable polymorph under ambient conditions.

31

### 32 **Keywords**

33 Benzylthiouracil; Dimorphism; Crystallographic properties; Thermodynamic properties; Pressure-temperature  
34 phase diagram; physical stability

## 35 1 INTRODUCTION

36 Benzylthiouracil (BTU), of which the molecular formula is shown in **Figure 1**, is an active pharmaceutical  
37 ingredient (API) for drugs against hyperthyroidism (also Graves-Basedow disease) through the inhibition of  
38 thyroid hormone production. A first report of its crystal structure was published in 1986 by Delage et al.  
39 (Delage et al., 1986) in which some hydrogen atom coordinates are missing. The CIF is available under the  
40 reference FICBEY in the Cambridge Structural Database (CSD) (See Supplementary Information, **Table S1**). A  
41 different dataset (space group and lattice parameters) was presented in a conference by Halder one year later  
42 (Halder, 1987) leading to the conclusion that BTU is at least dimorphic. However, while reporting that the unit-  
43 cell contains two independent molecules, the author did not publish the complete crystal structure. Available  
44 crystallographic information in the literature has been compiled in **Table 1**. Very little other solid-state  
45 information can be found in the literature on BTU. In the current paper, the structure found by Delage will be  
46 called form II and the one found by Halder will be called form I.

47 The information on the solid state of BTU is incomplete, while formulations with the API exist on the market.  
48 In fact, after examination and recrystallization of commercial batches of BTU, two crystalline forms were  
49 found. Besides a lack in information concerning the crystal structures, it is not clear which of the two forms is  
50 more stable at room temperature and which of them would therefore be the most appropriate choice to use  
51 in a drug formulation. Therefore, both crystal structures have been solved once again to complete the  
52 structural data. Furthermore, the thermal expansion of the two polymorphs has been determined so that their  
53 specific volumes can be calculated as a function of the temperature.

54 To determine which of the two forms is stable at room temperature, calorimetric measurements have been  
55 carried out. This system is a prime example of a solid-solid transition temperature that changes as a function  
56 of the DSC heating rate and therefore the transition cannot easily be related to the equilibrium temperature  
57 between the two solid forms (Barrio et al., 2012; Li et al., 2020; Toscani et al., 2016). In the case of benfluorex-  
58 HCl, it was possible to use the heating rate of the DSC to find a transition temperature that is consistent with  
59 the pressure-temperature phase diagram (Barrio et al., 2012). However, in other cases, such as pyrazinamide  
60 and piracetam, this was less evident (Li et al., 2020; Toscani et al., 2016).

61 Finally, a pressure-temperature phase diagram has been constructed, which considerably facilitates the  
62 necessary evaluations that are carried out in drug development to determine whether the compound may be  
63 sensitive to transformation during processing by grinding (heating of the sample) or by tableting (pressure  
64 increase) for example. The phase diagram constructed in this paper is a so-called topological pressure-  
65 temperature phase diagram, which can be calculated with the specific volumes of the known polymorphs as a  
66 function of the temperature (thermal expansion) and a sufficient number of equilibrium temperatures and  
67 transition enthalpies for the involved phases. If the topological phase diagram leads to doubts in relation to  
68 possible transformations of the API during processing or storage, further tests can be carried out on the drug  
69 molecule. If on the other hand, the phase equilibria are not in the proximity of any processing conditions, a  
70 topological phase diagram can be a quick way to rule out the immediate need for more technically demanding  
71 experiments.

## 72 2 MATERIALS AND METHODS

### 73 2.1 BENZYLTHIOURACIL SAMPLES

74 Benzylthiouracil of medicinal grade (purity > 99.0 %) was kindly provided by Bouchara-Recordati Laboratories,  
75 France, and used as such.

### 76 2.2 SCANNING ELECTRON MICROSCOPY

77 Electron microscopy images have been obtained using a Hitachi TM-1000 (Japan) tabletop scanning electron  
78 microscope with a scanning voltage of 15 kV. To improve the quality of the sample images, the samples were  
79 coated with a thin layer of gold.

### 80 2.3 HIGH RESOLUTION X-RAY POWDER DIFFRACTION

81 Powder X-ray diffraction (PXRD) was carried out on a transmission mode diffractometer using the  
82 Debye-Scherrer geometry equipped with cylindrical position sensitive detectors (CPS120) from INEL (France)  
83 containing 4096 channels (0.029° 2 $\theta$  angular step) with monochromatic Cu K $\alpha_1$  ( $\lambda$  = 1.5406 Å) radiation.  
84 Specimens were introduced into a 0.5 mm diameter Lindemann capillary, which during the measurements was

85 rotating perpendicularly to the X-ray beam to improve the average over the crystallite orientations. External  
86 calibration using the  $\text{Na}_2\text{Ca}_2\text{Al}_2\text{F}_{14}$  cubic phase mixed with silver behenate was performed by means of cubic  
87 spline fittings.

## 88 2.4 SINGLE CRYSTAL X-RAY DIFFRACTION

89 Single-crystal X-ray diffraction (SC-XRD) data were recorded on a Bruker Smart Apex single crystal  
90 diffractometer. A molybdenum  $\mu\text{S}$  microfocus X-ray source was used, running at 50 kV and 0.6 mA, emitting  
91  $\text{Mo-K}\alpha$  radiation ( $\lambda = 0.710731 \text{ \AA}$ ). A charge-coupled device (CCD chip 4K, 62mm) area detector was positioned  
92 at 6.0 cm.

93 For both crystalline forms, the orientation matrices and unit cells were established using the APEX2 (v2014.11-  
94 0) program suite (Sheldrick, 2014). The 3D reflection profile and the integration of all reflections were  
95 processed with SAINT (v8.34A) (Sheldrick, 2014). SADABS (v2014/5)(Sheldrick, 2014) was used to correct for  
96 Lorentz and polarization effects and for absorption due to the sample. The SHELXTL (v2014/7) program suite  
97 (Sheldrick, 2014) was used to solve the structure by the intrinsic phasing method and to refine the solution by  
98 full-matrix least-squares calculations on  $F^2$  (Sheldrick, 2014). All hydrogen atoms were located using a Fourier  
99 difference map and subsequently included in the refinement with one overall isotropic thermal parameter.

100 An Oxford Cryosystems nitrogen cryostat (Cryostream Plus) was used to control the temperature during single  
101 crystal X-ray diffraction experiments at various temperatures ranging from 80 K up to 400 K.

## 102 2.5 DIFFERENTIAL SCANNING CALORIMETRY

103 Differential scanning calorimetry (DSC) was used to obtain the peak onset temperature and heat of transition.  
104 A Q100 thermal analyser from TA Instruments was used and various heating rates were applied. The analyser  
105 was calibrated using the melting point of indium ( $T_{\text{fus}} = 429.75 \text{ K}$  and  $\Delta_{\text{fus}}H = 28.45 \text{ J g}^{-1}$ ). The specimens were  
106 weighed using a microbalance sensitive to 0.01 mg and sealed in aluminium pans.

107

108

## 109 2.6 THERMOGRAVIMETRY

110 Thermogravimetric (TG) measurements were performed by means of a Q50 system from TA Instruments (USA)  
111 under nitrogen flux from room temperature to 550 K. Heating rates of 10 K·min<sup>-1</sup> and sample masses of ca. 5  
112 mg were used.

## 113 2.7 OPTICAL MICROSCOPY PHOTOGRAPHS AS A FUNCTION OF THE TEMPERATURE

114 Photographs of a single crystal of form II were taken with a Leica DMRB microscope while heating at a rate of  
115 10 K min<sup>-1</sup> using a Linkam TMS94 system as a temperature controller.

## 116 3 RESULTS

### 117 3.1 PREPARATION OF THE POLYMORPHS

118 Powder X-ray diffraction at room temperature was used to examine a number of BTU specimens. Some of the  
119 diffraction patterns matched the calculated pattern ascribed to form II, using the structure from the CIF FICBEY  
120 (CSD) of which the atom coordinates have been compiled in **Table S1**. Other specimens exhibited a different  
121 pattern, which was ascribed to form I after the full crystal structure had been determined from single-crystal  
122 X-ray diffraction (see below). A third group of specimens was found to be a mixture of forms I and II in varying  
123 ratios. In fact, a systematic observation of commercial batches by optical microscope allowed the selection of  
124 single crystals of both polymorphs that were suitable for single-crystal structure determination (see **Figure 2a**  
125 and **Figure S1** in the supplementary materials). In addition, by slow evaporation of a solution of BTU in acetone  
126 at 277 K, large crystals of form II were obtained in the bottom of the beaker, while on the walls of the beaker,  
127 a few small crystals of form I were observed too (**Figure 2b**). Moreover, the crystalline powders of pure form II  
128 were observed to transform into form I upon standing for months with an excess of either water or ethanol at  
129 room temperature.

### 130 3.2 STRUCTURE DETERMINATIONS FROM SINGLE-CRYSTAL X-RAY DIFFRACTION

131 The crystal structures of forms I and II have been determined using single crystals similar to those shown in  
132 **Figure 2a** and **b**. Concerning form I, the structure is the same as the one reported by Halder (Halder, 1987);

133 however, it has been refined using the standard space group  $P2_1/c$  instead of the non-standard setting  $P2_1/a$   
134 by switching parameters  $a$  and  $c$ . Crystal and experimental data have been compiled in **Table 2**. The fractional  
135 atom coordinates and isotropic displacement parameters for BTU form I at 296 K (space group  $P2_1/c$ ) have  
136 been compiled in **Table S2**. The fractional atom coordinates and isotropic displacement parameters for form II  
137 at 297 K (space group  $P2_1/c$ ) have been compiled in **Table S3**. X-ray crystallographic information files (CIFs) can  
138 be obtained free of charge from the Cambridge Crystallographic Data Centre (CCDC), deposit numbers  
139 2045868 (form I) and 2045660 (form II) via [www.ccdc.cam.ac.uk/data\\_request/cif](http://www.ccdc.cam.ac.uk/data_request/cif). The geometrical features  
140 (bond lengths and bond angles) of the molecules in the two structures can be found in these files. Atom labels  
141 for the two independent molecules of form I can be found in **Figure S2** in the supplementary materials.

### 142 3.3 THERMODYNAMIC ANALYSIS WITH RESULTS FROM THERMOGRAVIMETRY, DIFFERENTIAL 143 SCANNING CALORIMETRY, AND HOT STAGE MICROSCOPY

144 DSC curves demonstrate that the II $\rightarrow$ I transition is endothermic (**Figure 3a**); however, the onset temperature  
145 of the transition depends on the heating-rate (see **Figure S3** in the supplementary materials for hot-stage  
146 microscopy photographs). After the solid-solid transition, fusion of form I is observed (**Figure 3a**). TG analysis  
147 demonstrates that no weight loss occurs on heating below 510 K (**Figure 3b**). The latter finding is independent  
148 of the polymorph.

149 On heating forms I or II at rates below or equal to 10 K $\cdot$ min<sup>-1</sup>, the mean melting temperature of form I was  
150 found to be  $T_{I\rightarrow L} = 496.8 \pm 1.0$  K (**Figure 4**). By extrapolating the heating rate to 0 K $\cdot$ min<sup>-1</sup> in **Figure 4**, the  
151 equilibrium temperature between form II and form I is expected to be  $T_{II\rightarrow I} = 405.4 \pm 1.0$  K. In addition, the  
152 mean value of the heat of fusion of form I was found to be  $152.6 \pm 4$  J $\cdot$ g<sup>-1</sup> and the mean value of the heat of the  
153 II $\rightarrow$ I transition was found to be  $5.6 \pm 1.5$  J $\cdot$ g<sup>-1</sup> (see the values in **Tables S4a and S4b** in the supplementary  
154 materials).

### 155 3.4 THERMAL EXPANSION OF BENZYLTHIOURACIL FORMS I AND II

156 Unit-cell metrics and symmetry have been determined isothermally at temperatures ranging from 80 K to 400  
157 K for form I and 80 K to 296 K for form II with the same single crystals as used for the structure resolutions. The  
158 specific volumes of the two forms, shown in **Figure 5**, have been calculated with the lattice parameters

159 compiled in **Tables S5a and S5b** in the supplementary materials. These results were fitted to the following  
160 quadratic functions with  $\nu$  in  $\text{cm}^3\cdot\text{g}^{-1}$  and  $T$  in K:

$$161 \quad \nu_{\text{I}} = 0.7167(7) + 4.36(60) \times 10^{-5} T + 1.2(1) \times 10^{-7} T^2 \quad (r^2 = 0.9994) \quad (1)$$

$$162 \quad \nu_{\text{II}} = 0.7201(7) + 4.47(90) \times 10^{-5} T + 1.2(2) \times 10^{-7} T^2 \quad (r^2 = 0.9995) \quad (2)$$

## 163 4 DISCUSSION

### 164 4.1 CRYSTAL STRUCTURES

165 In contrast to the structure of form II, form I contains two independent molecules in its asymmetric unit ( $Z' =$   
166 2), as previously mentioned by Halder (Halder, 1987). These two molecules (A and B in **Figure S2** in the  
167 supplementary materials) possess two different conformations (**Figure 6**) caused by the different orientations  
168 of the heterocycle with respect to the aromatic ring. In molecule A, the torsion angles N2A-C4A-C5A-C6A and  
169 C4A-C5A-C6A-C7A are equal to  $176.41^\circ$  and  $97.80^\circ$ , respectively, while angles N1B-C4B-C5B-C6B and C4B-C5B-  
170 C6B-C7B are  $-77.71^\circ$  and  $-50.53^\circ$ , respectively, in molecule B (see atom labels in **Figure S2**).

171 The molecules form infinite linear chains parallel to the  $a$  axis (see **Figure S4** in the supplementary materials).  
172 Molecules A and B participate in hydrogen-bonded 'dimers' through pseudo-cycles alternatingly made of pairs  
173 of N—H $\cdots$ O and N—H $\cdots$ S bonds, as shown in **Figure 7**. The distances and angles of these hydrogen bonds are  
174 listed in **Table S6** in the supplementary information in which those for form II are listed for comparison.

175 In contrast to form I, only one independent molecule is present in the asymmetric unit of the structure of form  
176 II, as previously found by Delage et al. (Delage et al., 1986). In **Figure 8**, one can see how centro-symmetric  
177 hydrogen-bonded dimers are formed through N-H $\cdots$ O hydrogen bonds (see **Table S6**). A 3D network exists  
178 with bifurcated hydrogen bonds linking the dimers to each other.

### 179 4.2 THE PRESSURE-TEMPERATURE PHASE DIAGRAM

180 It has been established that the monovariant, two-phase equilibrium lines in a pressure-temperature state  
181 diagram are straight lines over a considerable range of temperatures and pressures, in particular within the

182 ranges applicable to APIs (Ceolin et al., 2017). Therefore, using the Clapeyron equation to determine the  
183 slopes in a pressure-temperature phase diagram ( $dP/dT$ ), these equilibria can be extrapolated as straight,  
184 monotonically rising lines. These curves are the projections on the pressure-temperature plane of the  
185 monotonic Gibbs-energy surface intersections reflecting the absolute stability of the phases in a one-  
186 component system.

187 The Clapeyron equation, in the form  $dP/dT = \Delta H/T\Delta V$ , requires the enthalpy change and the change in specific  
188 volume,  $\Delta H$  and  $\Delta V$ , determined at the temperature  $T$  at which the two-phase equilibrium is located for a  
189 given pressure  $P$ , most often ordinary pressure. In the case of BTU, the following quantities have been  
190 obtained from the measurements and results discussed above:

191  $T_{II \rightarrow I} = 405.4(1.0)$  K,  $\Delta_{II \rightarrow I}H = 5.6(1.5)$  J·g<sup>-1</sup>,  $T_{I \rightarrow L} = 496.8(1.0)$  K, and  $\Delta_{I \rightarrow L}H = 152.6(4.0)$  J·g<sup>-1</sup>.

192 Other transition data such as for the melting of form II,  $T_{II \rightarrow L}$  and  $\Delta_{II \rightarrow L}H$ , and the volume changes such as  $\Delta_{II \rightarrow L}V$   
193 can be obtained by calculation. The enthalpy of fusion of form II is found to be  $\Delta_{II \rightarrow L}H = 158.2 \pm 4.2$  J·g<sup>-1</sup> using  
194 Hess's law by adding  $\Delta_{II \rightarrow I}H$  to  $\Delta_{I \rightarrow L}H$  and neglecting the difference in specific heat between the two  
195 polymorphs. The temperature of fusion of form II can be found using a modification of the relationship  
196 proposed by Yu (Yu, 1995) to provide the temperature of fusion of one of the polymorphs (Gana et al., 2013):

197 
$$T_{II \rightarrow L} = \frac{\Delta_{I \rightarrow L}H + \Delta_{II \rightarrow I}H}{\frac{\Delta_{I \rightarrow L}H}{T_{I \rightarrow L}} + \frac{\Delta_{II \rightarrow I}H}{T_{II \rightarrow I}}} \quad (3)$$

198 This leads to a melting temperature for form II of  $492.9 \pm 1.4$ K.

199 The volume change associated with the II→I transition is negative:  $\Delta_{II \rightarrow I}V = v_I - v_{II} = -0.0036$  cm<sup>3</sup>·g<sup>-1</sup> at  $T_{II \rightarrow I}$   
200 from eqs. 1 and 2. The volume change on melting of form I cannot be calculated directly, because the specific  
201 volume of the liquid is not known. Liquid volumes of APIs are often difficult to determine due to degradation in  
202 the liquid state or at high temperatures even in the solid state. Nonetheless, with statistical information about  
203 the volume change on melting of small organic molecules including APIs, it has been found that the mean ratio  
204  $v_{\text{liquid}}/v_{\text{solid}}$  between the specific volume of the liquid and that of the highest melting polymorph at its  
205 temperature of fusion equals 1.11 (Barrio et al., 2019; Ceolin and Rietveld, 2017; Céolin and Rietveld, 2015;  
206 Goodman et al., 2004; Rietveld and Céolin, 2015).

207 Using eq. 1, the specific volume of form I at fusion (496.8 K) can be calculated leading to  $0.7684 \text{ cm}^3 \cdot \text{g}^{-1}$ . For  
208 the liquid, this leads to  $v_{\text{liquid}} = 0.8529 \text{ cm}^3 \cdot \text{g}^{-1}$  at  $T_{\text{I} \rightarrow \text{L}}$  and a volume change on melting of  $\Delta_{\text{I} \rightarrow \text{L}} v = 0.0845 \text{ cm}^3 \cdot \text{g}^{-1}$ .

209 Using the inequalities and temperatures that have been obtained experimentally or by calculation,  $dP/dT_{\text{II} \rightarrow \text{I}}$   
210 and  $dP/dT_{\text{I} \rightarrow \text{L}}$  can now be calculated leading respectively to  $-3.82 \text{ MPa} \cdot \text{K}^{-1}$  and  $3.63 \text{ MPa} \cdot \text{K}^{-1}$ .

211 Taking the vapor pressure as 0 MPa for the II→I transition and for the fusion of form I, the calculated slopes  
212 can be used to extrapolate the equilibrium lines from the respective transition temperatures obtained by DSC.

213 The equations for the two equilibrium curves, I-II and the fusion of form I, become:

$$214 \quad P_{\text{II} \rightarrow \text{I}} / \text{MPa} = -3.82 T / \text{K} + 1548 \quad (4)$$

$$215 \quad P_{\text{I} \rightarrow \text{L}} / \text{MPa} = 3.63 T / \text{K} - 1806 \quad (5).$$

216 Calculating the intersection of these two equations, leads to the coordinates of the I-II-liquid triple point with  
217 the triple point temperature equal to 450 K and the pressure equal to  $-170 \text{ MPa}$ .

218 The equilibrium curve of the fusion of form II will pass through the triple point II-liquid-vapor obtained by  
219 calculation above. The temperature is equal to 492.9 K and once again taking the pressure at this point equal  
220 to 0 MPa, which can be done because of the steepness of the slope associated with this equilibrium, the  
221 equation of the equilibrium curve of the fusion of form II can be calculated using the coordinates of the I-II-L  
222 triple point. This leads to the following expression:

$$223 \quad P_{\text{II} \rightarrow \text{L}} / \text{MPa} = 3.97 T / \text{K} - 1956 \quad (6).$$

224 With the equations 4, 5, and 6, a preliminary pressure-temperature phase diagram has been drawn (**Figure 9a**)  
225 containing the stable phase regions for the condensed phases. It demonstrates that forms I and II exhibit their  
226 own stability domains: form II at lower temperature and form I at higher temperature. It can also be observed  
227 that the stable phase region of form I expands towards lower temperatures as the pressure increases, in  
228 accordance with the Le Chatelier principle (transition II→I is shifted right on heating since it is endothermic  
229 and favoured by a pressure increase, since form I is denser than form II). The phase relationship between the  
230 two forms is therefore enantiotropic.

231 Taking into account the vapor phase, the topological P-T phase diagram in **Figure 9b** has been drawn, while  
232 making sure that the two-phase equilibrium curves obey the stability alternation rule around each triple point.  
233 One can see that two of the four triple points are stable (I-II-vapor and I-liquid-vapor), and two others are  
234 metastable (II-liquid-vapor and I-II-liquid) corresponding to a case of overall enantiotropic behaviour,  
235 previously described by Bakhuis-Roozeboom as case 2 among the four possible cases of pressure-temperature  
236 phase diagrams describing dimorphism (Bakhuis Roozeboom, 1901; Ceolin and Rietveld, 2016; Ceolin et al.,  
237 2008).

## 238 5 CONCLUDING REMARKS.

239 The crystal structures of the two known forms of benzylthiouracil have been redetermined and in the case of  
240 form I, a full crystallographic description has been provided with atom coordinates. As far as the high-  
241 temperature form I is concerned, the crystal structure was found to be the same as solved by Halder, which  
242 remained unpublished up to now (Halder, 1987).

243 These two structures illustrate the conformational versatility of the benzylthiouracil molecule, which can  
244 adopt at least three conformations, two found in form I and another in form II. They are shown in **Figure 10**  
245 with the benzene ring of each molecule superimposed to demonstrate the relative position of the heterocycle.  
246 This dimorphism is once again another case of conformational polymorphism (Bernstein and Hagler, 1978;  
247 Négrier et al., 2013).

248 Concerning the thermodynamic aspect of this case of dimorphism, it has been shown that the reconstructive  
249 transition from form II to form I occurs on heating at a heating-rate dependent onset temperature. The fusion  
250 of form I is observed at a relatively high temperature of 496.8 K, as a result of strong hydrogen-bonding. It is  
251 accompanied with a high melting enthalpy of  $152.6 \text{ J}\cdot\text{g}^{-1}$  ( $33.31 \text{ kJ}\cdot\text{mol}^{-1}$ ) with respect to a generally observed  
252 melting enthalpy of about  $100 \text{ J}\cdot\text{g}^{-1}$  for small molecular compounds, although the similarly aromatic  
253 pyrazinamide also possesses a high melting enthalpy of  $241 \text{ J}\cdot\text{g}^{-1}$  ( $29.67 \text{ kJ}\cdot\text{mol}^{-1}$ ), while its melting temperature  
254 is lower with 462 K (Li et al., 2020).

255 The dependence of the solid-solid transition temperature between the two polymorphs on the DSC heating  
256 rate is a warning not to limit an investigation to a single heating rate as the transition temperature may not

257 reflect the actual equilibrium temperature at all. In the case of BTU, it appears that extrapolating its transition  
258 behaviour to zero heating rate leads to a reliable estimate of the equilibrium temperature as the dependency  
259 levels off at low heating rates. Nonetheless, such measurements should always be done with care.

260 The topological pressure-temperature phase diagram, constructed with the help of the Clapeyron equation  
261 using enthalpy and volume changes measured at ordinary pressure, corresponds to a case of overall  
262 enantiotropy. Even if the  $dP/dT$  slope of the II-I equilibrium curve is negative, each phase possesses its own  
263 stable phase region at pressures relevant for stable organic compounds and APIs. This diagram demonstrates  
264 that form II is clearly the stable polymorph under ambient conditions. However, temperatures during  
265 processing will need to remain below 400 K and even lower if grinding or tableting is used.

#### 266 **Funding**

267 This work has partially been supported by the Spanish Ministry of Science and Innovation Project FIS2017-  
268 82625-P and by the Generalitat de Catalunya Project 2017 SGR-042.

#### 269 **Declarations of Interest**

270 None

#### 271 **Acknowledgements**

272 The authors are grateful to Drs Marc-Antoine Perrin and Benoît Robert for their helpful support and fruitful  
273 discussions.

#### 274 **Supplementary material**

275 Supplementary data is available online and contains atom coordinates of the original structure published by  
276 Delage (Table S1), optical microscopy photographs of crystals in commercial batches (Figure S1), atom  
277 coordinates of form I in setting  $P2_1/c$  (Table S2), atom labels of benzylthiouracil for form I (Figure S2), atom  
278 coordinates in form II (Table S3), optical microscopy photos of the solid-solid transition (Figure S3),  
279 calorimetric data on the II-I and I-L transitions (Table S4), lattice parameters as a function of the temperature  
280 for forms I and II (Table S5), a figure of the linear hydrogen-bonded chains in form I (Figure S4) and a Table on  
281 the hydrogen-bond characteristics (Table S6).

282 **References**

- 283 Bakhuis Roozeboom, H.W., 1901. Die heterogenen Gleichgewichte vom Standpunkte der Phasenlehre.  
284 Erstes Heft: Die Phasenlehre - Systeme aus einer Komponente. Friedrich Vieweg und Sohn, Braunschweig.
- 285 Barrio, M., Allouchi, H., Tamarit, J.L., Ceolin, R., Berthon-Cedille, L., Rietveld, I.B., 2019. Experimental and  
286 topological determination of the pressure-temperature phase diagram of racemic etifoxine, a  
287 pharmaceutical ingredient with anxiolytic properties. *Int. J. Pharm.* 572, 118812.
- 288 Barrio, M., Maccaroni, E., Rietveld, I.B., Malpezzi, L., Masciocchi, N., Ceolin, R., Tamarit, J.L., 2012. Pressure-  
289 temperature state diagram for the phase relationships between benfluorex hydrochloride forms I and II: a  
290 case of enantiotropic behavior. *J. Pharm. Sci.* 101, 1073-1078.
- 291 Bernstein, J., Hagler, A.T., 1978. Conformational polymorphism. The influence of crystal-structure on  
292 molecular-conformation. *J. Am. Chem. Soc.* 100, 673-681.
- 293 Ceolin, R., Rietveld, I.-B., 2016. X-ray crystallography, an essential tool for the determination of  
294 thermodynamic relationships between crystalline polymorphs. *Ann. Pharm. Fr.* 74, 12-20.
- 295 Ceolin, R., Rietveld, I.B., 2017. The topological phase diagram of cimetidine: A case of overall monotropy.  
296 *Ann. Pharm. Fr.* 75, 89-94.
- 297 Céolin, R., Rietveld, I.B., 2015. The topological pressure-temperature phase diagram of ritonavir, an  
298 extraordinary case of crystalline dimorphism. *Ann. Pharm. Fr.* 73, 22-30.
- 299 Ceolin, R., Tamarit, J.L., Barrio, M., Lopez, D.O., Nicolai, B., Veglio, N., Perrin, M.A., Espeau, P., 2008. Overall  
300 monotropic behavior of a metastable phase of biclotymol, 2,2'-methylenebis(4-chloro-3-methyl-  
301 isopropylphenol), inferred from experimental and topological construction of the related P-T state  
302 diagram. *J. Pharm. Sci.* 97, 3927-3941.
- 303 Ceolin, R., Toscani, S., Rietveld, I.B., Barrio, M., Tamarit, J.-L., 2017. Pitfalls and feedback when constructing  
304 topological pressure-temperature phase diagrams. *Eur. Phys. J. - S.T.* 226, 1031-1040.
- 305 Delage, C., H'Naifi, A., Goursolle, M., 1986. Etude structurale du benzyl-6 thio-2 uracile C<sub>11</sub>H<sub>10</sub>N<sub>2</sub>O<sub>2</sub>S et  
306 considérations conformationnelles. *C.R. Acad. Sci., Ser. IIC: Chim.* 303, 1645-1650.
- 307 Gana, I., Barrio, M., Do, B., Tamarit, J.-L., Céolin, R., Rietveld, I.B., 2013. Benzocaine polymorphism:  
308 Pressure-temperature phase diagram involving forms II and III. *Int. J. Pharm.* 456, 480-488.
- 309 Goodman, B.T., Wilding, W.V., Oscarson, J.L., Rowley, R.L., 2004. A note on the relationship between  
310 organic solid density and liquid density at the triple point. *J. Chem. Eng. Data* 49, 1512-1514.

311 Halder, A., 1987. Studies of nucleobases and their derivatives : crystal structures of 6-benzyl-2-thio uracil  
312 (C<sub>11</sub>H<sub>10</sub>N<sub>2</sub>O<sub>2</sub>S), 5-iodo-1-methyl uracil (C<sub>5</sub>H<sub>5</sub>N<sub>2</sub>O<sub>2</sub>). Acta Crystallogr. A43.

313 Li, K., Gbabode, G., Barrio, M., Tamarit, J.-L., Vergé-Depré, M., Robert, B., Rietveld, I.B., 2020. The phase  
314 relationship between the pyrazinamide polymorphs  $\alpha$  and  $\gamma$ . Int. J. Pharm. 580, 119230.

315 Négrier, P., Barrio, M., Tamarit, J.L., Mondieig, D., Zuriaga, M.J., Perez, S.C., 2013. Conformational  
316 Polymorphism: the missing phase of 1,1,2,2-tetrachloroethane (Cl<sub>2</sub>HC-CHCl<sub>2</sub>). Cryst. Growth Des. 13,  
317 2143-2148.

318 Rietveld, I.B., Céolin, R., 2015. Phenomenology of crystalline polymorphism: overall monotropic behavior  
319 of the cardiotonic agent FK664 forms A and B. J. Therm. Anal. Calorim. 120, 1079-1087.

320 Sheldrick, G.M., 2014. APEX2 Software Suite for Crystallographic Programs. Bruker AXS Inc., Madison, WI,  
321 USA.

322 Toscani, S., Céolin, R., Ter Minassian, L., Barrio, M., Veglio, N., Tamarit, J.-L., Louër, D., Rietveld, I.B., 2016.  
323 Stability hierarchy between piracetam forms I, II, and III from experimental pressure-temperature  
324 diagrams and topological inferences. Int. J. Pharm. 497, 96-105.

325 Yu, L., 1995. Inferring Thermodynamic Stability Relationship of Polymorphs from Melting Data. J. Pharm.  
326 Sci. 84, 966-974.

327

328

329 **Figure Captions**

330 **Figure 1.** Molecular formula of benzylthiouracil, IUPAC name: 6-Benzyl-2-thioxo-2,3-dihydro-4(1H)-  
331 pyrimidinone,  $C_{11}H_{10}N_2OS$ ,  $M = 218.28 \text{ g mol}^{-1}$ .

332 **Figure 2. (a)** Electron microscopy photographs of single crystals of form I (left-hand side) and form II (right-  
333 hand side) selected from commercial batches of benzylthiouracil. **(b)** Optical microscopy photograph of  
334 crystals of form II grown by slow evaporation in an acetone solution at 277 K. The white arrows indicate the  
335 presence of a few crystals of form I that appeared at the rim.

336 **Figure 3. (a)** Typical differential scanning calorimetry curves (endo up) for benzylthiouracil demonstrating that  
337 on heating form II transforms endothermically to form I, which melts subsequently, and **(b)** a corresponding  
338 thermogravimetric curve demonstrating that weight loss only occurs once the sample is melting.

339 **Figure 4.** The transition of benzylthiouracil form II into form I (solid circles) and the onset temperatures of the  
340 fusion of form I (open diamonds) as a function of the heating rate.

341 **Figure 5.** The specific volumes of benzylthiouracil form I (solid squares) and form II (open circles) as a function  
342 of the temperature.

343 **Figure 6.** Molecular conformations in benzylthiouracil form I. Molecule A is blue and molecule B is red with  
344 atoms labelled A and B in **Table S2** and **Figure S2**, respectively. The two phenyl rings are superimposed  
345 emphasizing the difference in the orientation of the heterocycles.

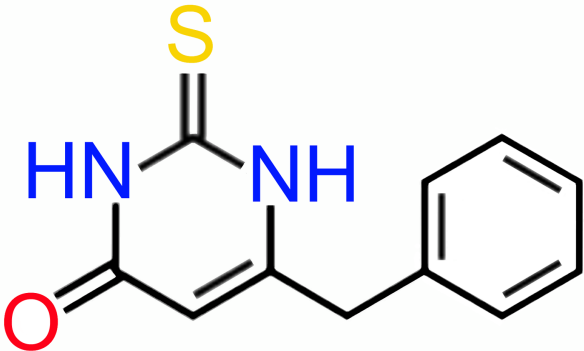
346 **Figure 7.** Hydrogen bonding in the structure of benzylthiouracil form I. Pseudo-cycles of non-centrosymmetric,  
347 hydrogen-bonded dimers with non-equivalent molecules A and B. Dimers A...B are formed by N—H...O (left-  
348 hand side) and N—H...S (right-hand side) hydrogen bonds (black: C, grey: H, blue: N, red: O, yellow: S).

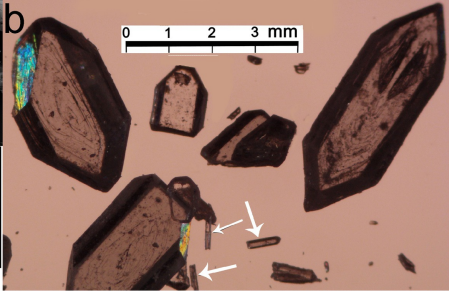
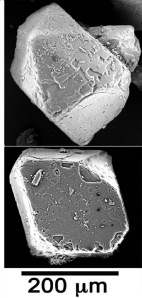
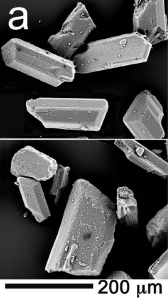
349 **Figure 8.** Hydrogen bonding in benzylthiouracil form II. A centrosymmetric dimer forms through two N1—  
350 H5...O1 hydrogen bonds. These dimers are linked by another hydrogen bond (N2—H4...O1) in such a way that  
351 atom O1 is linked to atoms N1 and N2 of two different molecules by a bifurcated hydrogen bond (angle N1—  
352 O1—N2 = 103.26°). The inversion centre is marked by the solid black point. The atom labels are the same as  
353 those in **Table S3** in the supplementary materials.

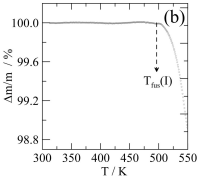
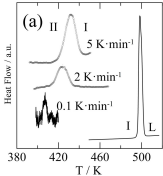
354 **Figure 9. (a)** The benzylthiouracil pressure-temperature phase diagram showing the stable regions of the  
355 condensed phases and the equilibrium curves involving forms I and II, and the liquid phase. **(b)** The full  
356 topological pressure-temperature phase diagram for the observed dimorphism of benzylthiouracil. Triple  
357 points: 1: I-liquid-vapor, 2: II-liquid-vapor, 3: I-II-vapor, and 4: I-II-liquid while solid black circles are stable and  
358 half black/half white circles are metastable; two-phase equilibrium lines: a-a: liquid-vapor, b-b: I-liquid, c-c: II-  
359 liquid, d-d: I-II, e-e: I-vapor, and f-f: II-vapor while black lines are stable equilibria, dashed lines are metastable,  
360 and open lines are super-metastable.

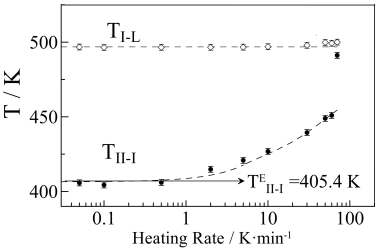
361 **Figure 10.** Conformational versatility of the benzylthiouracil molecule: the red and blue molecules are the  
362 conformations encountered in form I (**Figure 6**), whereas the yellow molecule represents the conformation in  
363 form II.

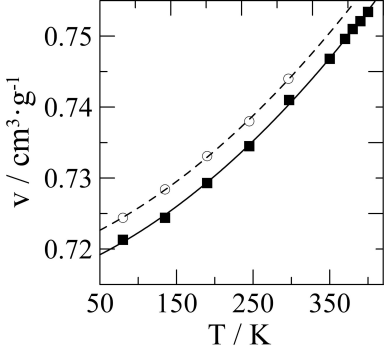
364

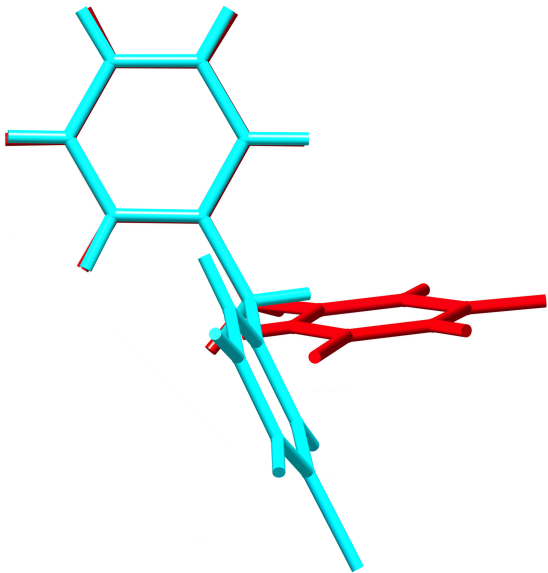


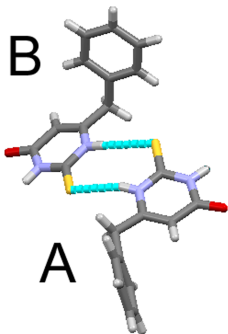
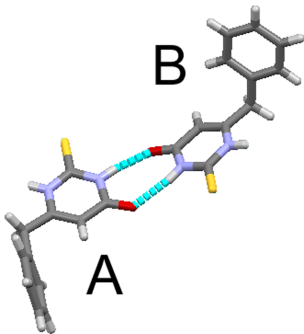


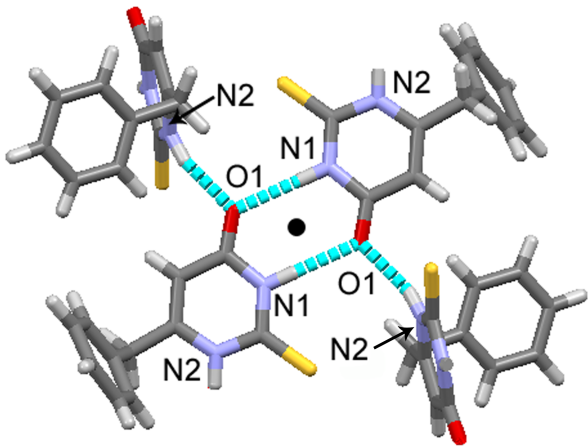


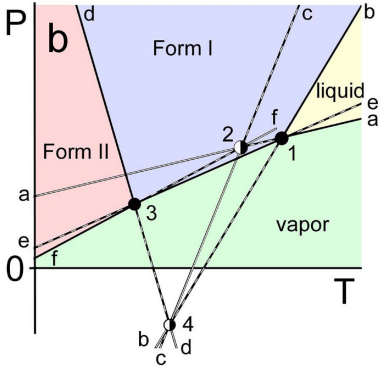
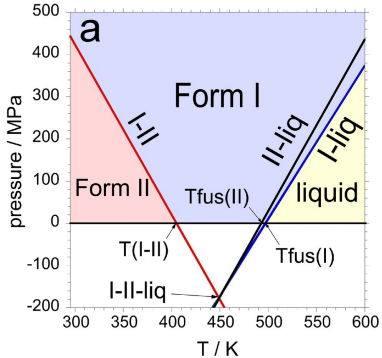












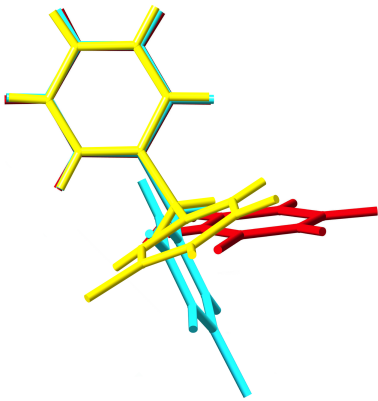


**Table 1. Benzylthiouracil crystallographic data at room temperature available in the literature**

Reference	(Halder, 1987)	(Delage et al., 1986)
Polymorph identification	Form I	Form II
Crystal system	Monoclinic	Monoclinic
Space group	P2 <sub>1</sub> /a	P2 <sub>1</sub> /c
a/Å	10.457(4)	9.735(1)
b/Å	20.131(6)	9.158(1)
c/Å	10.915(10)	12.519(1)
β/°	110.60(4)	106.81(1)
V(cell)/ Å <sup>3</sup>	2150.8	1068.42
Z	8	4
Z'	2	1
Density/g cm <sup>-3</sup>	1.3482	1.3570
Specific volume/cm <sup>3</sup> g <sup>-1</sup>	0.74171	0.73690
CSD reference	none	FICBEY

**Table 2. Crystal data and structure refinement for Forms I and II of benzylthiouracil<sup>a</sup>**

	Form I	Form II
Temperature ( $\sigma$ ) /K	296(2)	297(2)
Crystal system	monoclinic	monoclinic
Space group	<i>P2<sub>1</sub>/c</i>	<i>P2<sub>1</sub>/c</i>
<i>a</i> ( $\sigma$ ) /Å	10.9378(7)	9.7532(4)
<i>b</i> ( $\sigma$ ) /Å	20.1405(13)	9.1767(4)
<i>c</i> ( $\sigma$ ) /Å	10.4677(7)	12.5389(5)
$\beta$ ( $\sigma$ ) /°	110.683(1)	106.810(1)
Cell Volume ( $\sigma$ ) /Å <sup>3</sup>	2157(2)	1074.29(8)
<i>Z</i> / <i>Z'</i>	8 / 2	4 / 1
<i>M</i> /g·mol <sup>-1</sup>	218.27	218.27
<i>D</i> <sub>calc</sub> /g·cm <sup>-3</sup>	1.344	1.350
<i>V</i> <sub>calc</sub> /cm <sup>3</sup> ·g <sup>-1</sup>	0.74405	0.74074
$\mu$ (Mo <i>K</i> $\alpha$ ) /mm <sup>-1</sup>	0.273	0.274
<i>F</i> (000)	912	456
Crystal shape	rod-like	prism-like
Radiation /Å	Mo <i>K</i> $\alpha$ ( $\lambda$ = 0.71073)	Mo <i>K</i> $\alpha$ ( $\lambda$ = 0.71073)
$\theta$ range for data collection /°	1.990 to 28.999	2.794 to 29.075
Reflections collected	15865	10631
Independent reflections	5204 [ <i>R</i> <sub>int</sub> = 0.011, <i>R</i> <sub>sigma</sub> = 0.010]	2642 [ <i>R</i> <sub>int</sub> = 0.012, <i>R</i> <sub>sigma</sub> = 0.010]
Reflections with <i>I</i> > 2 $\sigma$ ( <i>I</i> )	4435	2487
No. parameters	351	176
Goodness-of-fit on <i>F</i> <sup>2</sup>	1.031	1.040
Final <i>R</i> indexes [ <i>I</i> ≥ 2 $\sigma$ ( <i>I</i> )]	<i>R</i> <sub>1</sub> = 0.0468, <i>wR</i> <sub>2</sub> = 0.1278	<i>R</i> <sub>1</sub> = 0.0475, <i>wR</i> <sub>2</sub> = 0.1400
Final <i>R</i> indexes [all data]	<i>R</i> <sub>1</sub> = 0.0478, <i>wR</i> <sub>2</sub> = 0.1288	<i>R</i> <sub>1</sub> = 0.0496, <i>wR</i> <sub>2</sub> = 0.1423
Largest diff. peak/hole / e·Å <sup>-3</sup>	0.552/-0.421	0.284/-0.210
CCDC	2045868	2045660

<sup>a</sup> estimated standard deviations in parentheses

